Combustion-Powered Actuation for Dynamic Stall Suppression – Simulations and Low-Mach Experiments

Claude G. Matalanis, Byung-Young Min, Patrick O. Bowles, Solkeun Jee, and Brian E. Wake,
United Technologies Research Center, East Hartford, CT

Tom Crittenden, George Woo, and Ari Glezer,
Georgia Institute of Technology, Atlanta, GA

claude.matalanis@utrc.utc.com

ABSTRACT

An investigation on dynamic-stall suppression capabilities of combustion-powered actuation (COMPACT) applied to a tabbed VR-12 airfoil is presented. In the first section, results from computational fluid dynamics (CFD) simulations carried out at Mach numbers from 0.3 to 0.5 are presented. Several geometric parameters are varied including the slot chordwise location and angle. Actuation pulse amplitude, frequency, and timing are also varied. The simulations suggest that cycle-averaged lift increases of approximately 4% and 8% with respect to the baseline airfoil are possible at Mach numbers of 0.4 and 0.3 for deep and near-deep dynamic-stall conditions. In the second section, static-stall results from low-speed wind-tunnel experiments are presented. Low-speed experiments and high-speed CFD suggest that slots oriented tangential to the airfoil surface produce stronger benefits than slots oriented normal to the chordline. Low-speed experiments confirm that chordwise slot locations suitable for Mach 0.3-0.4 stall suppression (based on CFD) will also be effective at lower Mach numbers.

INTRODUCTION[1]

Problems associated with dynamic stall continue to limit rotorcraft speed and efficiency. Retreating-blade stall (RBS) typically occurs between the blade mid-span and tip near the $\psi = 270°$ position. Although it commonly occurs on rotorcraft operating near the edge of their flight envelope, performance at these conditions plays an important role in rotor design as demand increases for faster and more agile rotorcraft with higher lift capacity. Furthermore, rotor blades are designed so that the extreme conditions at which stall occurs size key parameters such as blade chord.

The adverse effects of RBS can be mitigated through alleviation of dynamic stall at Mach numbers from 0.2 to 0.5. Previous work involving mechanical leading-edge slats, synthetic jets, and plasma actuation have shown some success, but each technique has its weaknesses or challenges (Refs. 1-4). Slats are very effective aerodynamically, however, overcoming advancing-side drag penalty has proven to be extremely difficult in terms of mechanical design. Synthetic jets and plasma actuation have shown significant promise across a range of speeds. Plasma actuation is the subject of several current research efforts, two of which are described in Refs. 5 and 6.

Combustion-powered actuation (COMPACT) provides a potential means for mitigating dynamic stall across a broad range of Mach numbers. COMPACT actuation can provide high-velocity, high-impulse jets for flow control from a small on-blade package (described in review in Ref. 7). In previous studies conducted at low Mach numbers, reattachment of separated flows has been demonstrated in a number of different airfoil configurations (e.g., Refs. 8-12).

The objective of this work is to evaluate the potential of COMPACT for mitigation of dynamic stall at higher Mach numbers between 0.2 and 0.5. The first portion of this paper focuses on high-speed dynamic stall simulations of a VR-12 airfoil equipped with COMPACT, and the second portion focuses on low-speed experiments performed in parallel on the same airfoil. Later in this program, it is planned to perform higher-speed dynamic-stall testing.

HIGH-MACH SIMULATIONS

Geometry and Methodology

The baseline airfoil selected for this study was a VR-12 with a 5% tab as shown in Figure 1. In the past, this airfoil has shown excellent stall characteristics (Ref. 13). Slots based on the COMPACT hardware used in the parallel experimental study were implemented on the upper surface near the leading-edge as shown in Figure 1. Slots oriented in the normal and tangential directions were investigated, and two chordwise locations were investigated, $x/c = 0.06$ and $x/c = 0.1$. The slot height, h/c, was approximately 0.0008. For the tangential slot, the slot angle is approximately 22°. For the normal slot, the jet direction is oriented perpendicular to the chordline of the airfoil. For the 3D geometry, each actuator extended 0.5” in the spanwise direction with a 3/16” wall between actuators. These dimensions were based on the experimental hardware.

[1]Presented at the American Helicopter Society 70th Annual Forum, Montréal, Québec, May 20-22, 2014.

Structured computational meshes used in this study were constructed using the commercially available Gridpro and Gridgen software packages in order to generate highly-efficient multi-block meshes suitable for 2D and 3D RANS simulations. Previous experimental studies have shown that the presence of the slot can impact the baseline dynamic stall characteristics of the airfoil (Ref. 14). With this in mind, as much detail of the slot geometry as possible was implemented in the computational mesh. Compact enrichment was used to increase mesh density at the leading and trailing edge of the airfoil. Boundary-layer clustering was applied along the airfoil surface and the sidewalls of the slot. 3D meshes were constructed with an identical topology near the airfoil, and a similar topology near the actuator. The actuator was modeled as finite in the spanwise direction with smooth transition between the slot and gap. In 2D, the domain extends 30 chord lengths into the farfield and is modeled with freestream boundary conditions. In 3D, the farfield was constructed to match the vertical extent of the NASA-Glenn Icing Research Wind Tunnel wherein experiments are planned. For simplicity, however, the walls were also modeled as freestream boundaries. Finally, the computational domain used consisted of half of one slot and half of one gap. This is illustrated by the close-up of the surface mesh at the actuator exit provided in Figure 3. In future studies where comparison with experiment will take place, boundary conditions at the tunnel walls will be modeled with greater fidelity.

The solver chosen for this study was CFL3D with the Spalart–Allmaras turbulence model, upwind biased third-order Roe scheme. Most cases presented in this work were run in 2D, however, select cases were run in 3D in an attempt to investigate the effects of a finite gap between slots and the effects of a skew angle to direct some of the pulse in the spanwise direction.

The variation in angle of attack was prescribed as $\alpha = \alpha_0 + \alpha_1 sin(\omega t)$, where reduced frequency, k, is defined as $\omega c/(2U_\infty)$ and selected to be representative of rotor conditions on the retreating side. Pulsing representative of COMPACT actuation was achieved using a time-dependent boundary condition which can accommodate high-frequency pulses with variable duration between pulses. The periods of time where pulsing was applied with respect to the pitch cycle are denoted as "half-cycle" and "quarter-cycle" with both of these illustrated in Figure 4. Pulsing frequency was based on measured data, and series of pulsations are continued during the periods of pulsing time.

Pulsing was implemented in CFL3D as follows. Pressure as a function of time for the COMPACT actuation was deduced from bench-top experiments performed at Georgia Tech wherein the chamber pressure was measured with respect to the ambient pressure. Many of these tests were performed at various flow-rates and pulsing frequencies. This pressure ratio measured ($P_r = P_{chamber}/P_{ambient}$) was used in combination with stagnation relations to calculate a Mach number to apply at the actuator face (bottom of the slot in the CFD grid). Velocities normal to the actuator face were set based on this Mach number. Pressure at the actuator face is extrapolated from the flow-field, and freestream temperature was applied.

For simplicity, a cosine function fit to the correct maximum value and duration was used to establish the time-dependent pressure ratio in CFL3D. The experimental data, however, matches this shape fairly well, as shown in Figure 5. To be conservative, the pressure ratio between pulses was dropped down to 1 in order to minimize passive blowing between pulses. The pressure ratio and frequency used for most of the simulations is denoted by the green point in Figure 6.

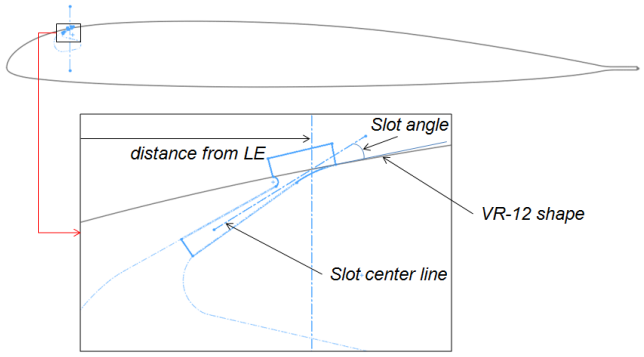

Figure 1. Tabbed VR-12 geometry with slot modifications.

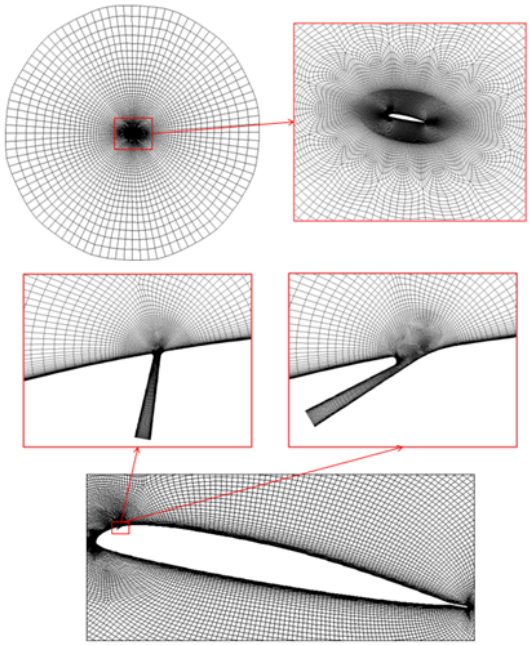

Figure 2. Computational meshes for normal and tangential slots.

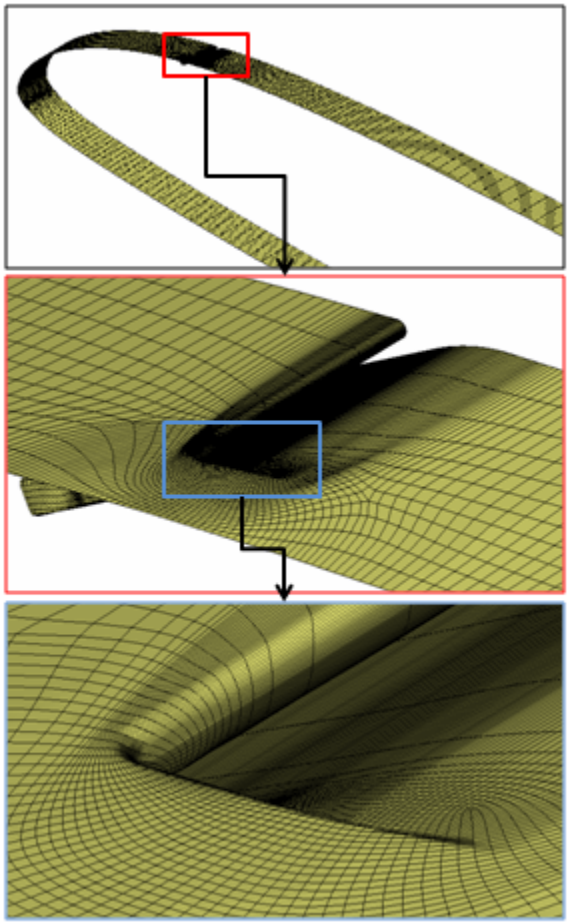

Figure 3. Surface mesh of 3D x/c=0.1 geometry illustrating slot/gap transition.

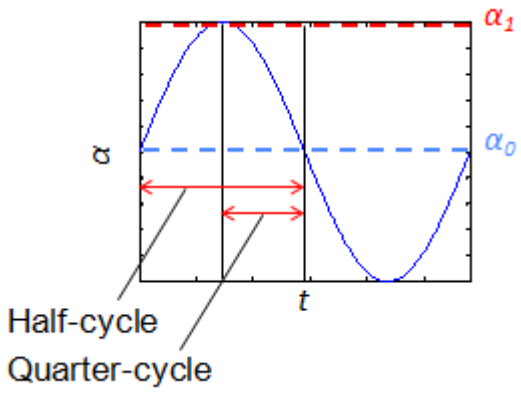

Figure 4. Pulsing strategies employed. During half-cycle or quarter-cycle durations shown here, pulses were fired at the frequencies and amplitudes specified in Figure 6.

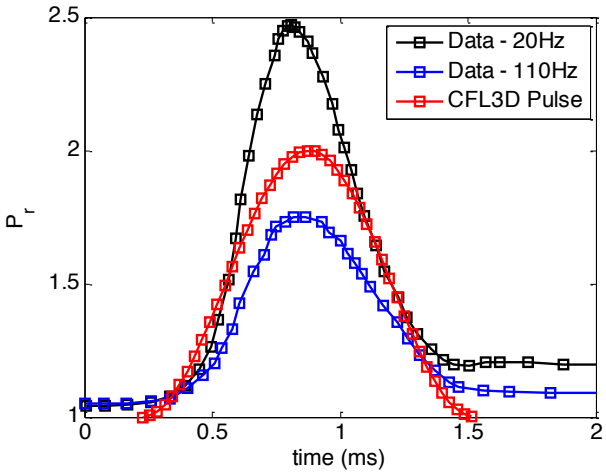

Figure 5. Sample data (Actuator C, 7 L/min) plotted with cosine function used to model pulse in CFL3D.

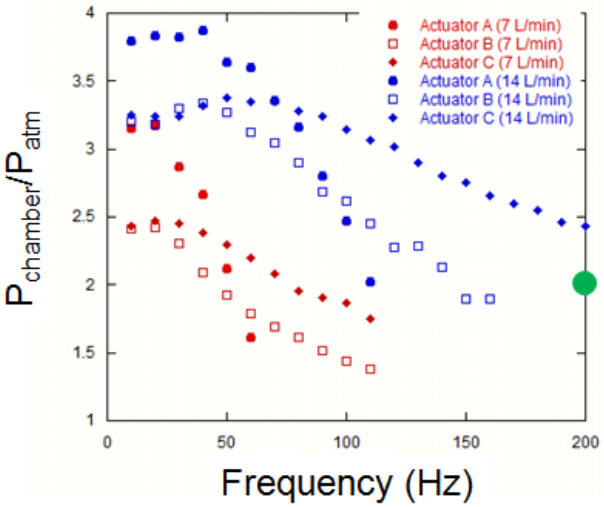

Figure 6. Plot from bench-top experiments illustrating the effects of pulsing frequency and flow-rate upon the peak pressure achieved. Actuators A, B, and C were three experimental design variations that were benchtop tested. Point shown in green indicates the pulsing used for most CFD cases.

Computational Results – 2D

To ensure adequately small grid-sensitivity, a grid refinement study was performed on the x/c=0.1 geometry at Mach 0.3 (Re_c = 2,600,000), α_0 = 10°, α_1 = 10°, k = 0.1. The main quantities of interest for this study are the changes in cycle-averaged lift ($\Delta C_{l,mean}$), cycle-averaged drag ($\Delta C_{d,mean}$), and peak negative moment ($\Delta C_{m,peak}$) due to pulsing. The nominal grid in addition to grids with half and double the resolution in each direction were run with and without pulsing to generate the results shown in Table 1. The changes in the main quantities of interest are small, and these results provide a good basis for the fidelity of the subsequent results. It was expected that peak negative moment would be a difficult quantity to accurately predict, and raw results for

this quantity (as provided in this work) are not considered highly reliable.

Table 1. 2D grid refinement results. Changes are relative to the slotted airfoil with no-pulsing.

	Coarse	Nominal	Fine
$\Delta C_{l,mean}$	0.080 (+7.6%)	0.087 (+8.1%)	0.091 (+8.4%)
$\Delta C_{d,mean}$	-0.033 (-36%)	-0.040 (-43%)	-0.040 (-43%)
$\Delta C_{m,peak}$	0.27 (-63%)	0.26 (-57%)	0.24 (-51%)

Results for x/c = 0.06 along with the clean airfoil and slotted (no blowing) cases run at Mach 0.3 (Re_c = 2,600,000), α_0 = 10°, α_1 = 10°, k = 0.1, are shown in Figure 7. Multiple lines for blowing cases represents blowing with different phase. First, it was shown that the differences between the slotted and clean airfoil were minimal, which was expected given the small chordwise extent of the slot. Second, it was shown that the tangential slot had a significantly higher impact on dynamic stall than the normal slot. Third, it was shown that varying the exact phase location of the pulse did not make a significant difference in the improvement seen. Note that the four phase locations attempted are with respect to the pulse-to-pulse phasing, not the pitch cycle. Finally, and most remarkably, the tangential slot half-cycle pulsing case (pulses occurring on first half of pitch cycle) showed a dramatic decrease in lift hysteresis, peak drag, and peak negative moment. Slightly better results (not shown here) were obtained at this Mach number when the slot placed at x/c = 0.1. The contours shown in Figure 8 illustrate that the actuation reduces the size of the stall separation, which is particularly visible 3/8 into the pitch cycle period (φ=3/8).

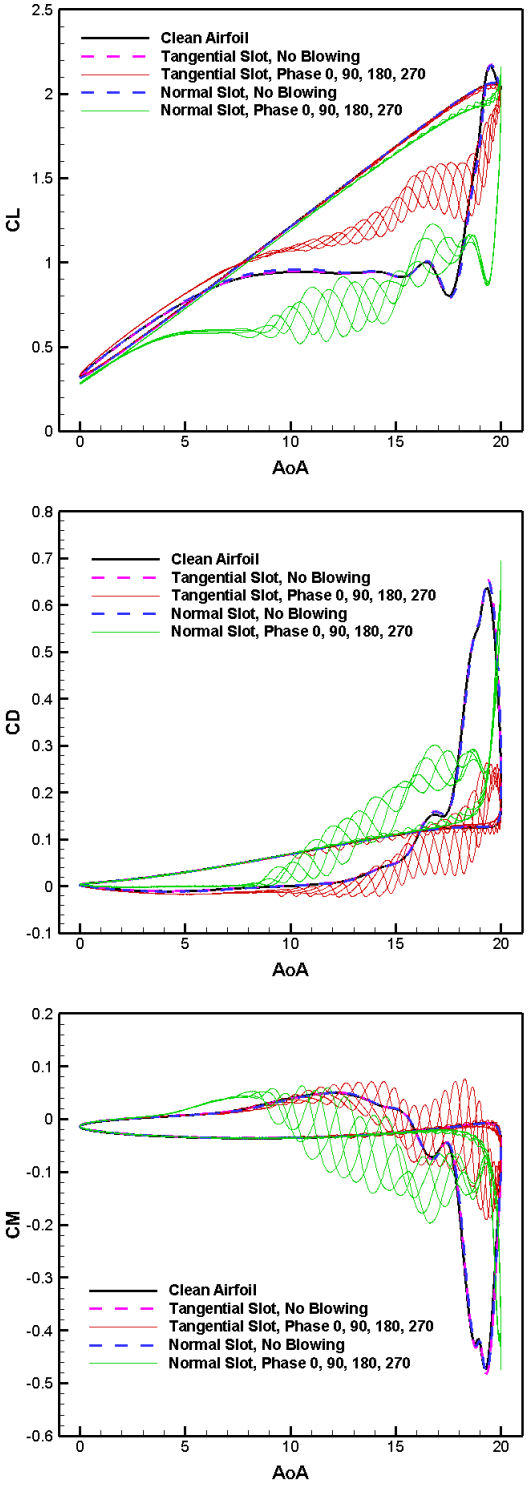

Figure 7. Lift, drag, and moment results for half-cycle pulsing with four variations in the pulse-to-pulse phasing for tangential and normal slots (Mach 0.3).

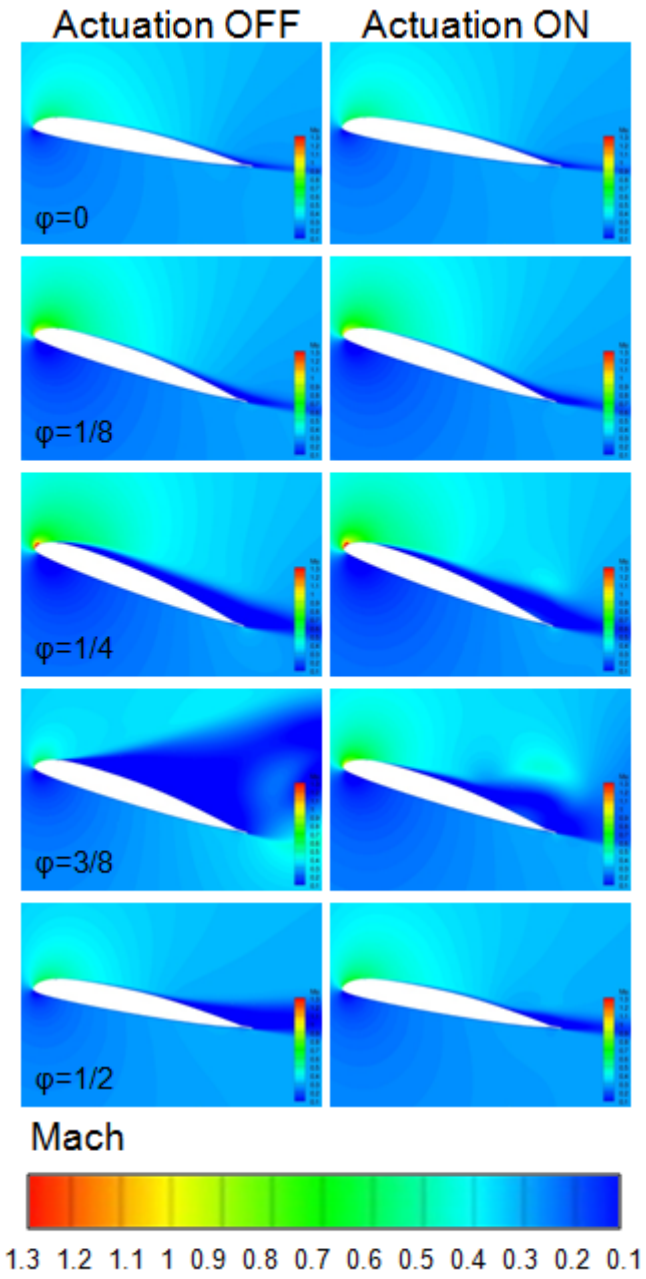

Figure 8. Mach contours for Mach 0.3, α_0 = 10°, α_1 = 10°, k = 0.1, illustrating the effect of actuation. First half of pitch cycle shown.

The same geometry was run at Mach 0.4 along with the *x/c* = 0.10 location, as shown in Figure 9. First, it was found that the presence of the *x/c* = 0.6 slot, indeed, has an effect on the baseline airfoil performance. An examination of the flowfield revealed that the slot at this location interacts with the shock formation. This interaction is avoided when the slot is placed at *x/c* = 0.1. For cases with actuation, it was also found that the x/c=0.1 location increases the benefits seen at Mach 0.4 while slightly increasing the benefits shown at Mach 0.3 as mentioned previously. Contours of Mach number about the airfoil and focused around the leading-edge are shown in Figure 10 and Figure 11. Two effects due to the actuation are noted. First, the actuation tends to decrease the size of the stall separation, similar to the effect noted at Mach 0.3. This is seen clearly at φ=1/4 and φ=3/8. Second, the strength of the shock upstream of the slot is increased, as shown at the same points in the pitch cycle.

All results shown thus far were produced with actuation frequencies and amplitudes set at the levels shown by the green point in Figure 6. It was of interest to determine the relative importance of these two parameters in order to guide future actuator development efforts. Figure 12 shows Mach 0.4 results for cases where the actuation frequency and amplitude were independently increased. The results suggest that increased amplitude or frequency may have a slight effect on the results but would not result in substantial changes in performance.

A summary of the benefits shown at each Mach number is provided in Figure 13. Results are also shown here for Mach 0.5 results; however, the effects at Mach 0.5, particularly in terms of cycle-averaged lift, appear to be limited.

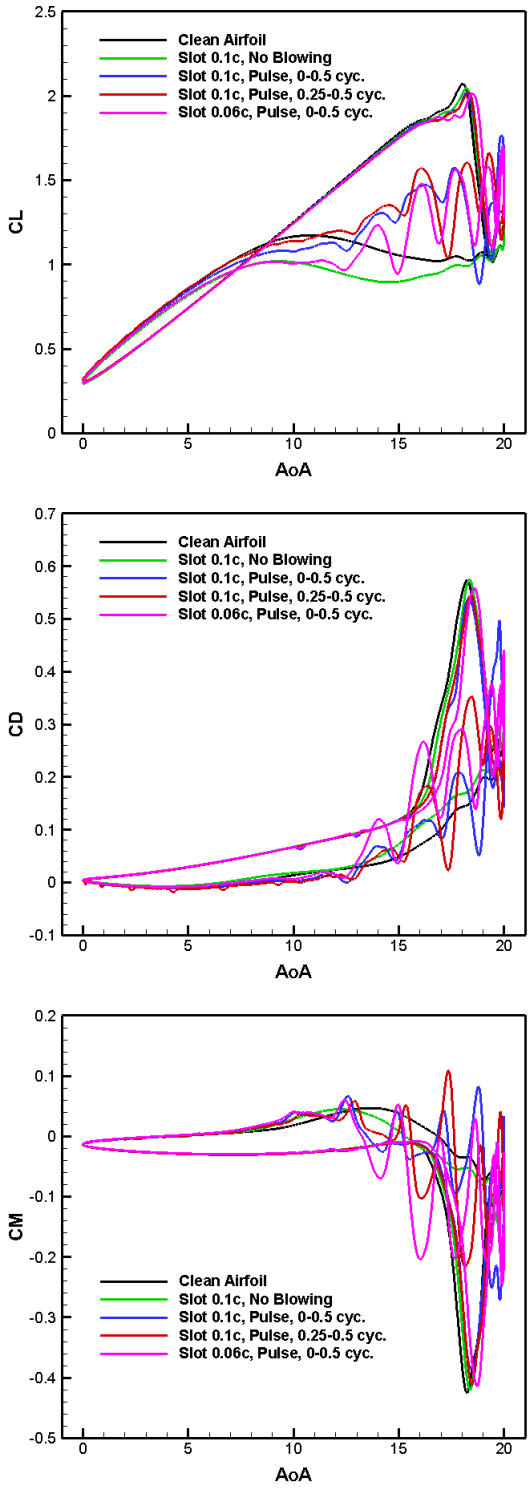

Figure 9. Lift, drag, and moment results for half-cycle pulsing with a tangential slot. Conditions are Mach 0.4, $\alpha_0 = 10°$, $\alpha_1 = 10°$, k = 0.07.

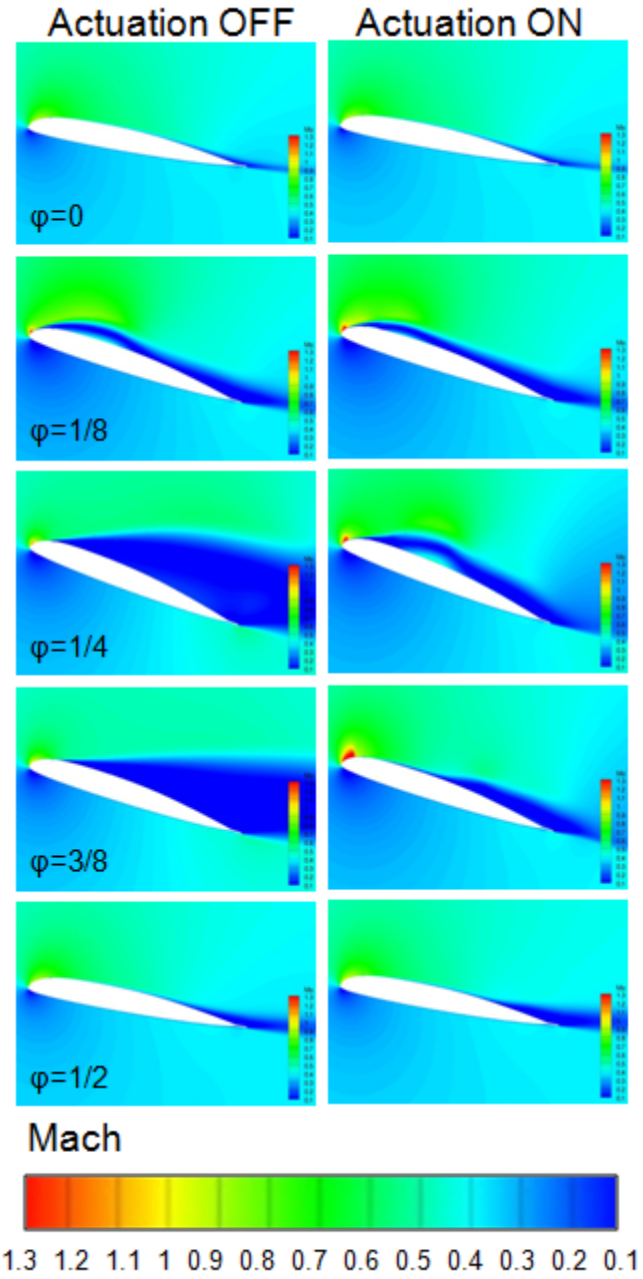

Figure 10. Mach contours for Mach 0.4, $\alpha_0 = 10°$, $\alpha_1 = 10°$, k = 0.07, illustrating the effect of actuation. First half of pitch cycle shown.

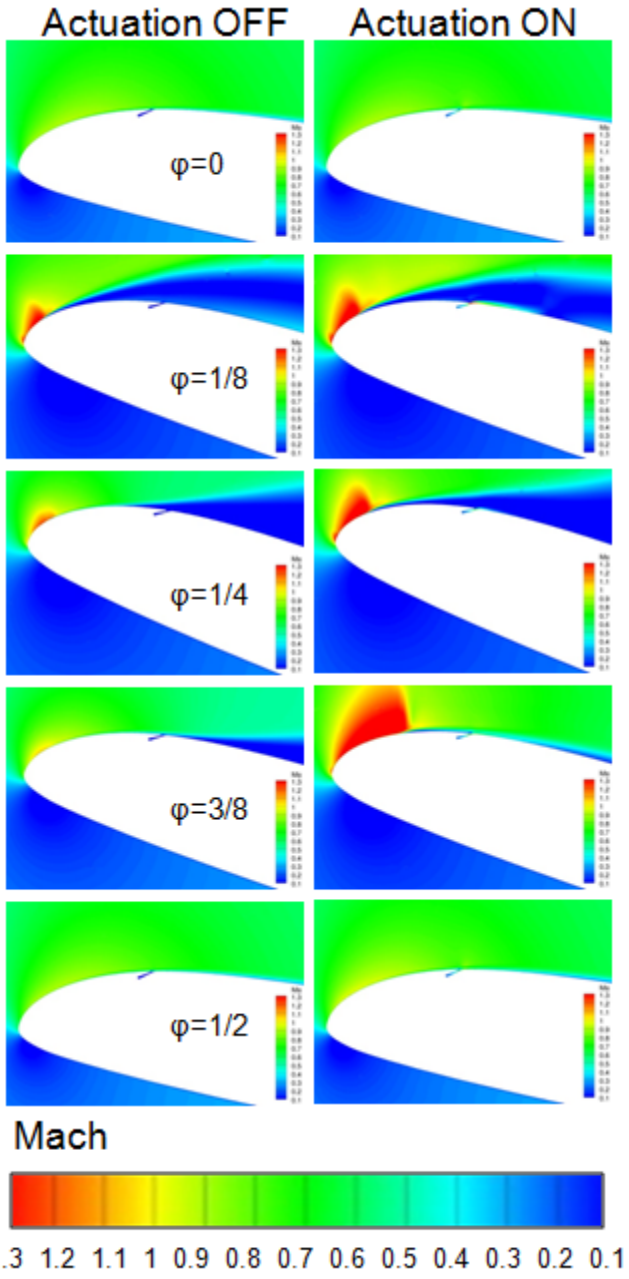

Figure 11. Mach contours for Mach 0.4, α_0 = 10°, α_1 = 10°, k = 0.07, illustrating the effect of actuation, focus on leading-edge. First half of pitch cycle shown.

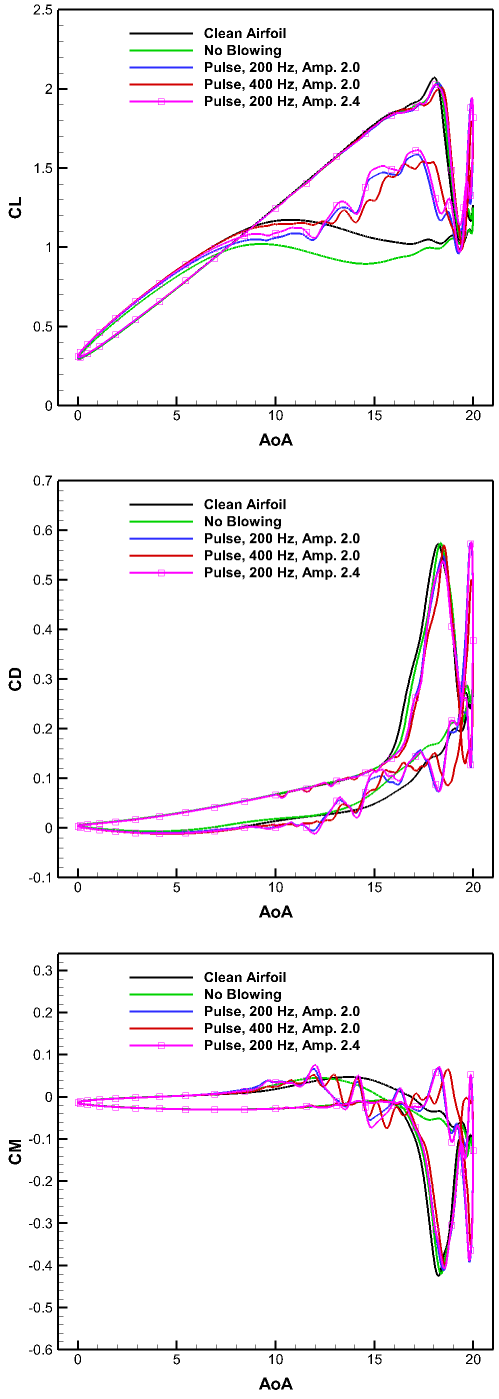

Figure 12. Lift, drag, and moment results for half-cycle pulsing with a tangential slot, pulsing parameter variations. Conditions are Mach 0.4, α_0 = 10°, α_1 = 10°, k = 0.07.

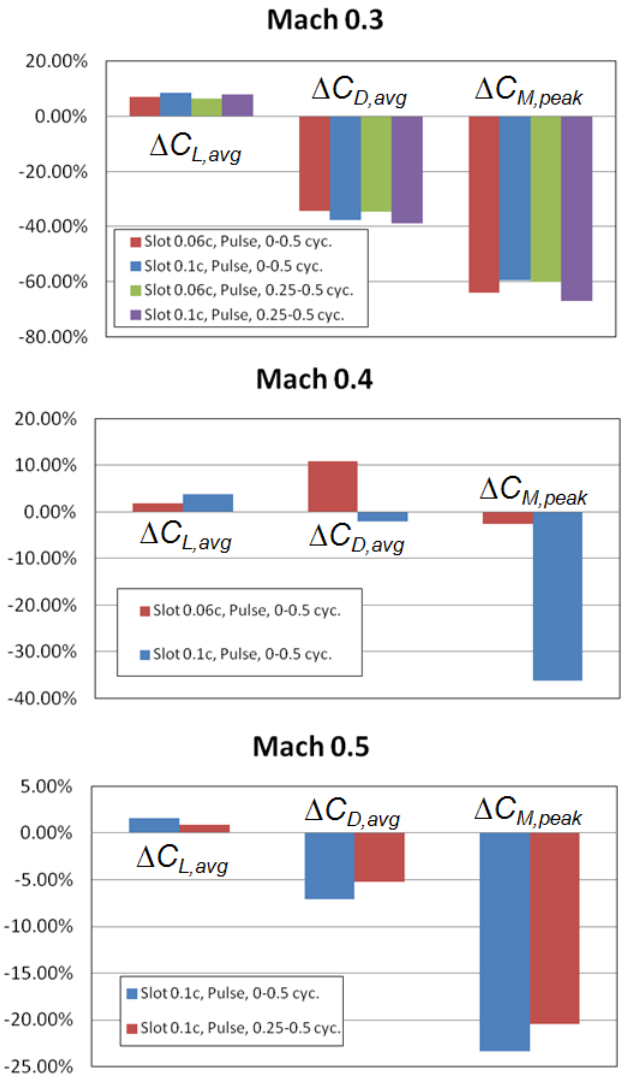

Figure 13. Summary of cycle-averaged quantities. Note that $\Delta C_{M,peak} < 0$ denotes a reduction in negative peak moment. Deltas are referenced to the clean airfoil except for Mach 0.5 which uses the slotted no-blowing case as reference. Note also that the Mach 0.5 pitch cycle constituted deeper stall penetration than the Mach 0.4 case.

Computational Results – 3D

The 3D studies performed focused on the $x/c = 0.1$ location and Mach 0.3 conditions. Similar to the 2D study, a grid refinement study was carried out to confirm adequately small grid sensitivity for the 3D grid. A comparison between the 2D and 3D simulations at $\alpha_0 = 10°$, $\alpha_1 = 10°$, $k = 0.1$, conditions is shown in Figure 14 and Table 2. As noted previously, the 3D geometry models the span of the slot as finite, and the slot ratio, $sr = L_{slot}/L_{span}$, is approximately 0.73. Differences between the 2D and 3D geometries for the no-pulsing cases can be at least partially attributed to the presence of the gap between actuators. However, given the sensitivity of dynamic stall simulation results to minute changes in the grids and grid topologies, numerical effects cannot be ruled out entirely.

An initial investigation was conducted to determine the potential for increasing the benefit by directing some of the jet momentum in the spanwise direction. The motivation for attempting this stems from the notion that some spanwise momentum from the jet may result in streamwise vorticity which would scale with the freestream velocity, thus, magnifying benefit at higher speeds.

In order to efficiently generate grids to carry out this investigation, the commercially available mesh-morphing software, Sculptor, was used to generate geometries with slots curved to a particular skew angle, β. This parameter is illustrated in Figure 15. The mesh-morphing technique eliminates the need to generate new meshes and produces new geometries with identical block topology.

The results of the skew angle study are shown in Figure 16. Focusing on the lift curves, it appears that the amount of lift hysteresis is reduced from the baseline (β=0) value as the skew angle is increased up to approximately 20°. It appears that the benefit resulting from a 30° angle is fairly close the the 20° result suggesting that beyond a certain point, further increases in slot skew angle are no longer beneficial.

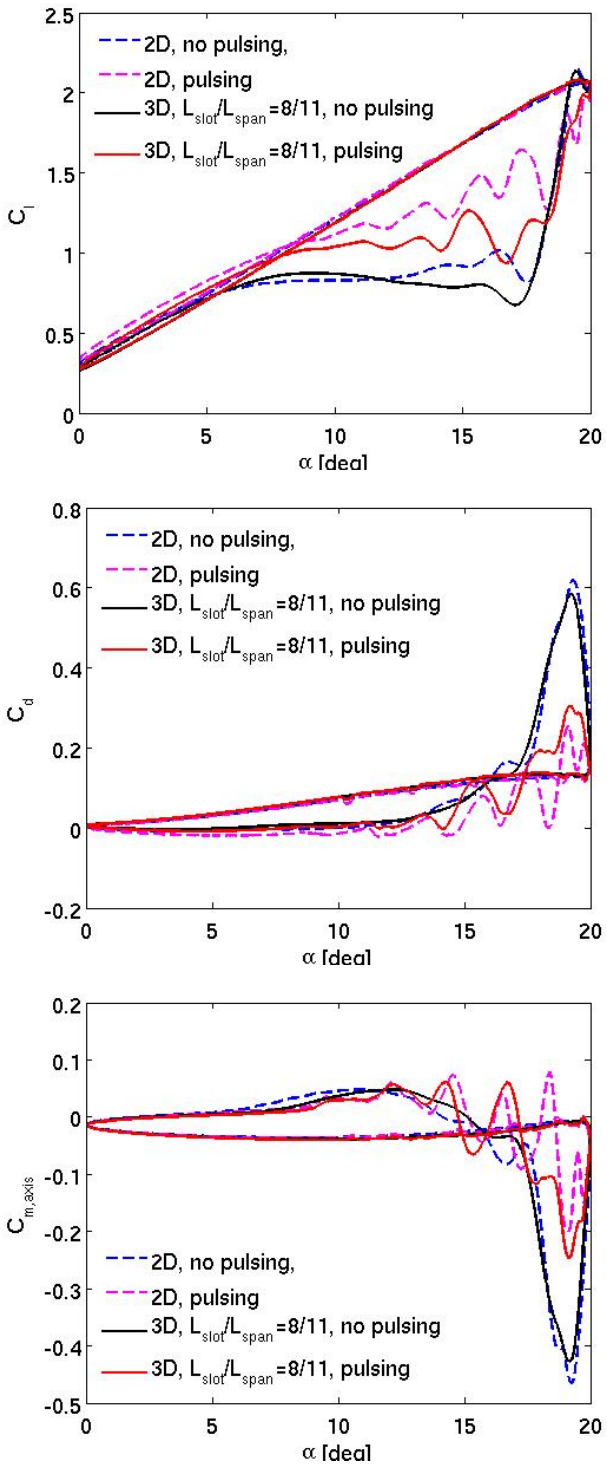

Figure 14. Comparison between 2D and 3D finite-span simulations. Conditions are Mach 0.3, α_0 = 10°, α_1 = 10°, k = 0.1.

Table 2. Comparison of half-cycle pulsing effectiveness based on 2D and 3D finite-span results. Conditions are Mach 0.3, α_0 = 10°, α_1 = 10°, k = 0.1.

	2D	3D: Finite Span Slot
$\Delta C_{l,mean}$	0.087 (+4.6%)	0.048 (+8.1%)
$\Delta C_{d,mean}$	-0.040 (-26%)	-0.025 (-43%)
$\Delta C_{m,peak}$	0.26 (-42%)	0.18 (-57%)

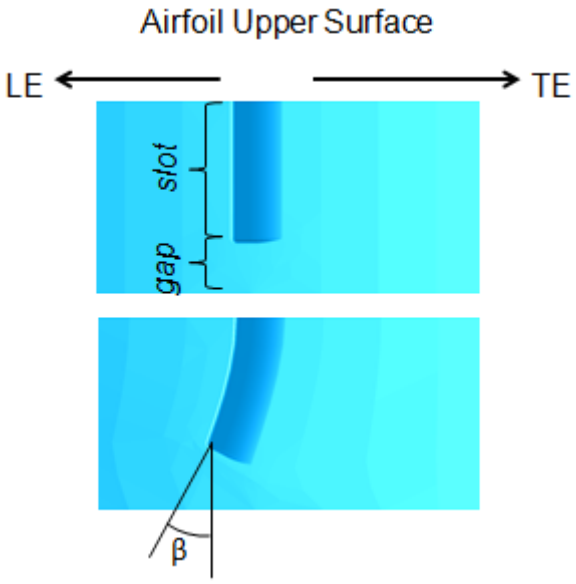

Figure 15. Top view of airfoil upper surface illustrating skew angle achieved via mesh-morphing.

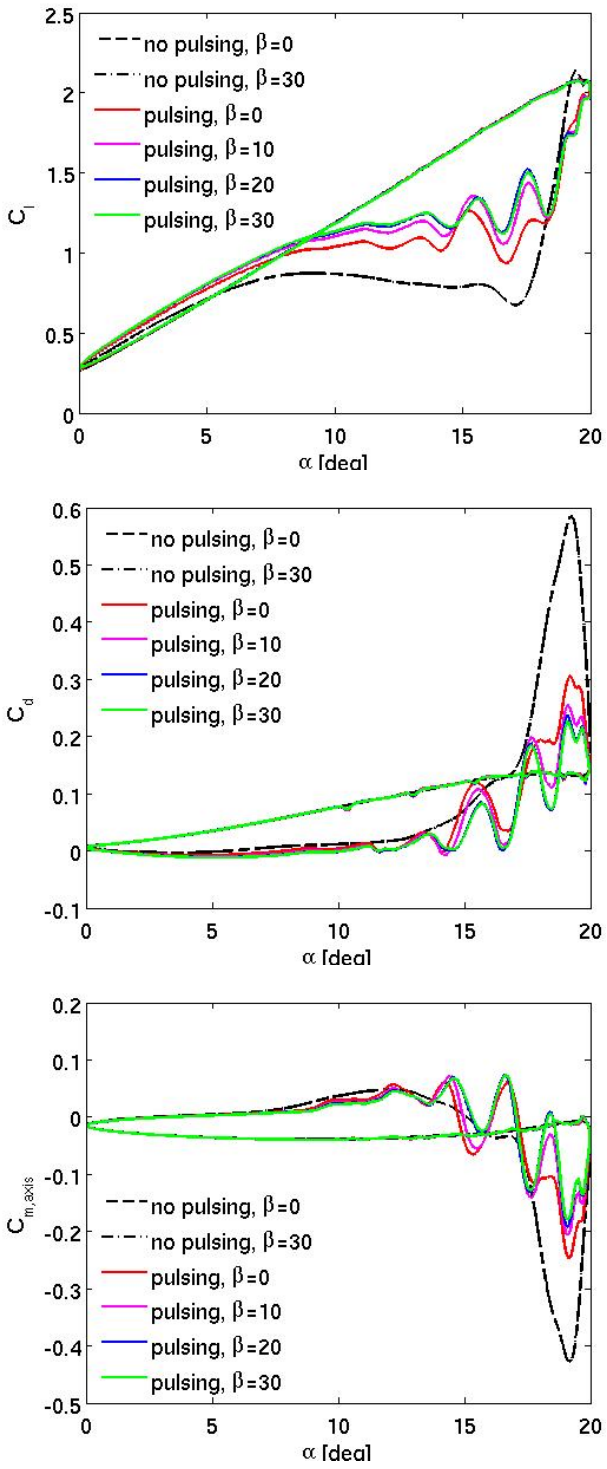

Figure 16. Lift, drag, and moment results for half-cycle pulsing with various several different skew angles. Conditions are Mach 0.3, $\alpha_0 = 10°$, $\alpha_1 = 10°$, k = 0.1

LOW-MACH EXPERIMENTS

Experimental Apparatus

As an initial test point, the effectiveness of COMPACT-based aerodynamic flow control for mitigation of stall on a static VR-12 airfoil was characterized in low-speed wind tunnel experiments at Georgia Tech. A new VR-12 wind tunnel model integrated with a spanwise array of COMPACT actuators was designed and constructed. The model has a chord $c = 0.381$ m and spans the full width of the tunnel's test section (nominally 91 cm). The model is mostly comprised of modular spanwise (8.9 cm wide) aluminum segments, each fabricated using 2-D wire-EDM. The segments are supported by an internal spar with matching, equally-spaced support cantilevers. The airfoil is assembled by bolting of the segments to the spar. The airfoil is mounted using two 2.54 cm dia, 3.5 mm thick hollow-tubes that are attached to the end segments of the model, and are designed for mounting the model on either existing static mounts or a dynamic 2-DOF traverse mechanism (Figure 17a). The model is equipped with a modular spanwise segment for measurement of surface pressure distributions (typically placed on the model centerline). The wire bundles, actuator feed lines and static pressure tubes are routed through the mounting tubes.

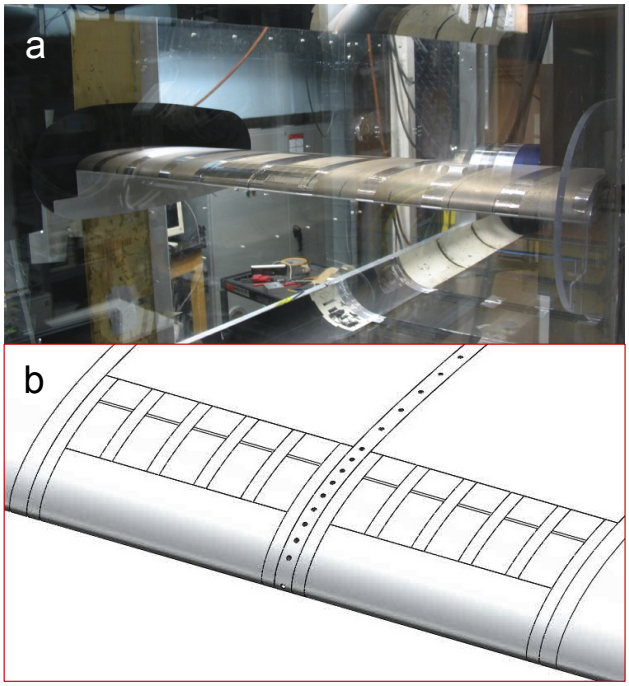

Figure 17. Low-speed VR-12 model mounted in Georgia Tech wind tunnel (a) and schematic view of actuator banks in leading edge (b).

The actuator section of the model includes two spanwise banks each having 5 interchangeable COMPACT actuators which are mounted on either side of the centerline (shown schematically in Figure 17b). Each actuator module has a nominally 0.35 mm wide slot which extends over the entire 1.27 cm span of the actuator. Individual actuators in each bank are separated by a 0.48 cm dividing plate. The gap between the adjacent actuator banks is 0.64 cm, and the overall span of the airfoil's active segment is 19 cm (or about 21% of the full span of the model). The new COMPACT actuator design is based on earlier benchtop investigations and is based on a contiguous internal combustor volume that

is designed to enhance mixing of the fuel and air. For the present experiments, two orifice geometries were fabricated exiting: ***i.*** normal to the model's chord line (about 80° relative to the local moldline, similar to earlier COMPACT installations on a NACA 4415 airfoil (see Refs. 10 and 11), and ***ii.*** nominally tangential at an angle of 20° relative to the moldline. Both orifice orientations are aligned to exit the airfoil at x/c=0.1.

Experimental Results

The performance of the COMPACT actuation for mitigation of stall was investigated at post-stall angles of attack of the static VR-12 model for 432,000 < Re < 875,000 (10.6 < T_{conv} < 21.4 msec). The baseline aerodynamic performance of the model was characterized in an earlier entry for angle of attack sweeps from -16° < α < 24° (with stall typically occurring near 16°). Fences were used only at the spanwise tips of the model (as pictured in Figure 17a), while the actuated segment of the model was unbounded and allowed to interact fully with the unactuated regions. The effects of the actuation were assessed using static pressure measurements along center span, and PIV measurements in the cross stream plane z = 0 (between the actuator banks) that were acquired phase-locked to the actuation pulse. A small (0.001c) trip wire was placed at 0.043c, upstream of the actuator slots. It is noteworthy that the trip was added to stabilize the point of separation, and, as discussed in connection with Figure 22, the actuation produces flow attachment even in the absence of the trip. Furthermore, in the present work, no attempt was made to optimize either the trip or actuation location.

A comparison between normal and tangential actuation is shown in circumferential distributions of the static pressure (Figure 18, Re=650,000, α=18°). The actuation is tested at three repetition rates as measured by the Strouhal number, $St_{act} \equiv f_{act} \cdot T_{conv}$ = 0.72, 1.07, and 1.43. The corresponding fuel/air flow rates to the actuators are 7 ("low"), 10.5 ("medium"), and 14 ("high") sL/min/actuator, respectively. In each run, the pressure distribution was measured in the absence of actuation, in the presence of steady air/fuel bleed only (without spark activation), and then with full, time-periodic actuation. As shown in Figure 18, in the absence of actuation, the flow is fully stalled (as it is for the baseline airfoil). These data show that the effects of normal and tangential actuation are somewhat different. While both actuation approaches result in full attachment at all St_{act}, the continuous bleed of the refill mixture has no effect with normal actuation, but it does alter the pressure distribution of the stalled flow when the actuation is tangential, indicating increased receptivity of the flow to tangential actuation. Nevertheless, it is anticipated that prohibitively high steady bleed flow rates would be necessary to replicate the attachment achieved with the transitory actuation effect by the COMPACT actuation.

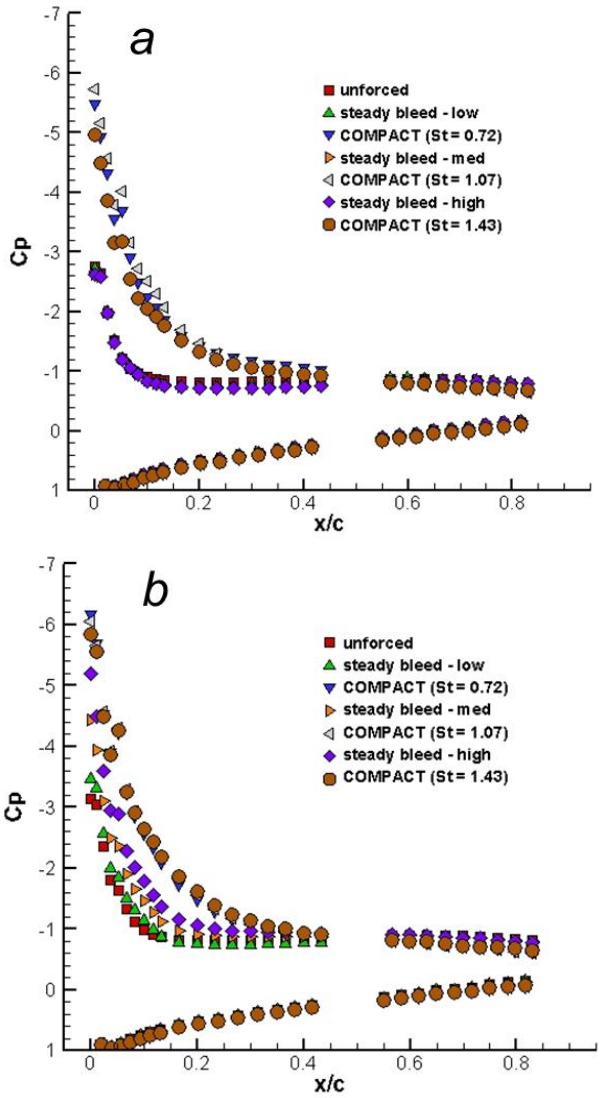

Figure 18. Static pressure distributions along the centerline for (a) normal actuation and (b) tangential actuation, (Re=650,000, α=18°) for three refill bleed rates and corresponding actuation repetition rates.

The comparative effectiveness of tangential actuation is considerably higher as the Reynolds number increases. At Re = 875,000 (Figure 19), the effect of normal actuation is rather limited and results in minor variations in the time-averaged pressure distribution indicating sporadic transient effects at best. However, tangential actuation leads to full attachment at all St_{act} (1.06, 0.8. 0.53), while the effect of continuous refill bleed is considerably diminished compared to the corresponding effects at lower Re (Figure 18). That the attachment is insensitive to the repetition rate of the actuation indicates that the inherently hysteretic effects of flow separation following pulse actuation are present, and that the flow does not separate within the repetition cycle. This is discussed in more detail in connection with Figure 20 below. Similar results were observed α = 20° (the maximum angle available with the static mounting configuration).

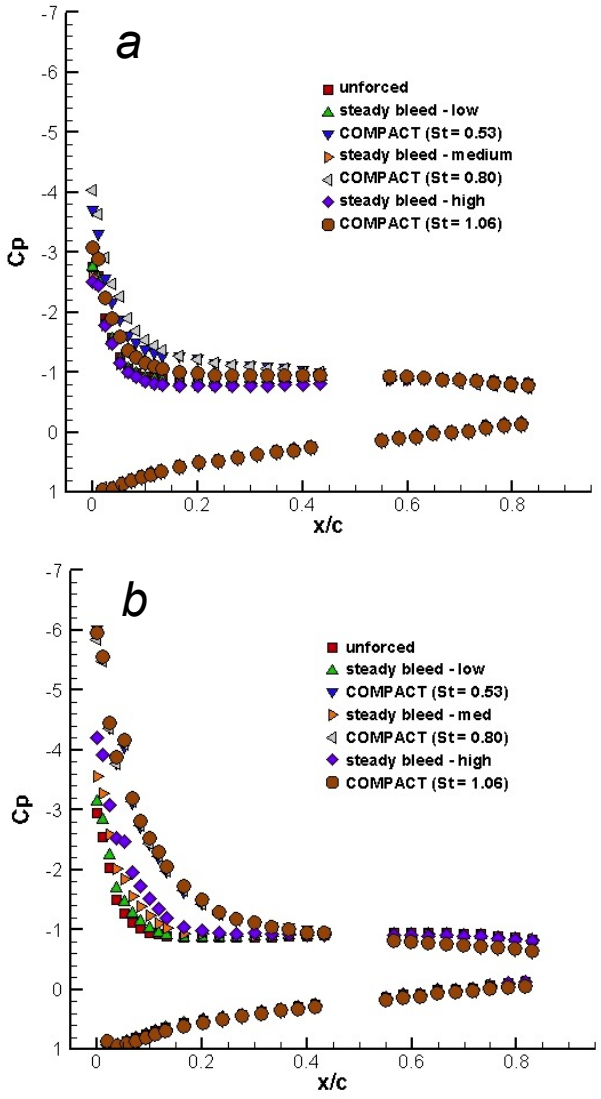

Figure 19. As in Figure 18 for Re = 875,000.

The flow structure during the repetition cycle was investigated using PIV measurements acquired phase-locked to the actuation pulse. For Re = 650,000, the attachment process for normal and tangential actuation is generally similar within the streamwise field of view ($0.34 < x/c < 1.05$) and so vorticity maps and velocity vectors are shown only for tangential actuation (Figure 20, $\alpha = 18^o$, $St_{act} = 0.72$, where the corresponding pressure data is shown in Figure 18b). It may be noted that the field of view here is limited by the mounting plate in the wind tunnel wall, with future experiments expected to include more comprehensive views of the flow dynamics near the actuator orifice. Figure 20a shows the large scale separation of the unforced flow, and exhibits reversed flow near the surface of the airfoil as is evidenced by the CCW vorticity concentration. Five phases during the repetition cycle t/T_{act} = 0.0, 0.1, 0.2, 0.3, and 0.4 (T_{act} is the repetition period) are shown in Figure 20b through f, respectively. The onset of the actuation ($t/T_{act} = 0$, Figure 20b) is demonstrated by the vorticity concentration near $x/c = 0.45$ that protrudes over the nominal boundary layer. It is noteworthy that while the boundary layer along the surface of the airfoil is relatively thick, there is virtually no evidence of reversed flow up to $x/c \approx 0.9$. Following the actuation ($T_{pulse} << Tc_{onv}$) the vortex that is formed by the actuation begins to grow and migrates downstream along the surface (t/T_{act} = 0.1, Figure 20c). A remarkable feature of this advection is that the boundary layter upstream of the vortex is considerably thinner that the boundary layer downstream of the vortex, indicating that the vortex induces an upstream favorable pressure gradient. This process continues as the vortex is advected all the way to the trailing edge (Figure 20c-f). Following the shedding of the vortex, the boundary layer begins to thicken and returns to its state prior to the next actuation pulse (in Figure 20b). This vortex shedding process is generally similar to that observed in previous COMPACT flow control demonstrations (Refs. 8-12). These data indicates that the timing between consecutive actuation pulses can be significantly lengthened before the flow may separate again (with measurable loss in lift) and therefore the repetition rate of the actuation can be significantly shortened with significant reduction in overall actuation power.

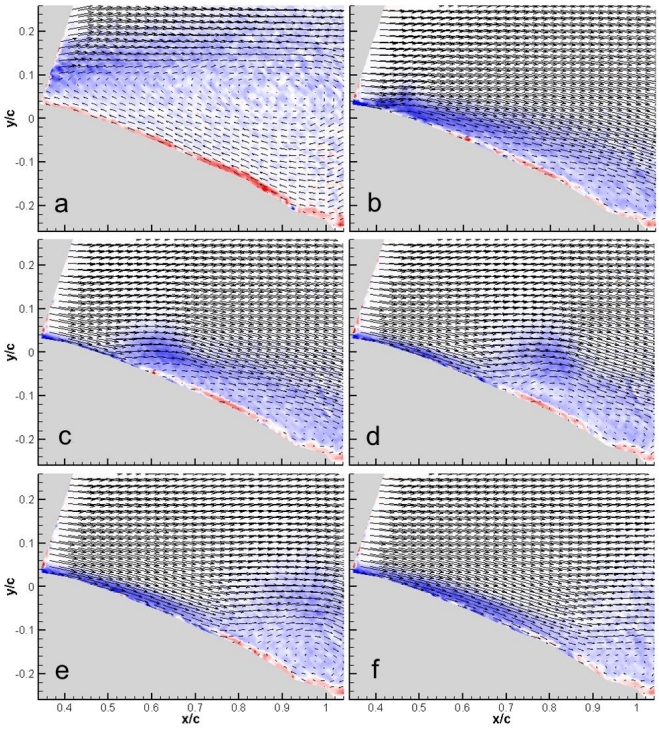

Figure 20. Phase-locked PIV measurements in the cross stream plane z = 0 for tangential actuation (Re=650,000, α=18°) showing, unforced flow (a) and at t/T_{act} =0 (b), 0.1 (c), 0.2 (d), 0.3 (e), and 0.4 (f).

This is further demonstrated in Figure 21 with centerline static pressures at lower repetition rates but with the air/fuel flow rate held invariant at the low level (tangential actuation, $\alpha = 18^o$, Re = 650,000 and 875,000). The pressure distributions for the unforced flow and steady refill bleed are shown for reference. At Re = 650,000, the pressure distributions for St_{act} = 0.29, 0.50, and 0.72 indicate fully attached flow and are nearly identical, and at $St_{act} = 0.14$

there is still significant partial attachment. Similar results were measured at Re = 875,000, with only slightly lower peak pressures attained at St_{act} = 0.27 and full attachment St_{act} = 0.37 and 0.53. The data indicate that full attachment can be achieved at St_{act} between 0.25 and 0.33. The effects of separation hysteresis can play a significant role in controlling the flow at higher speeds.

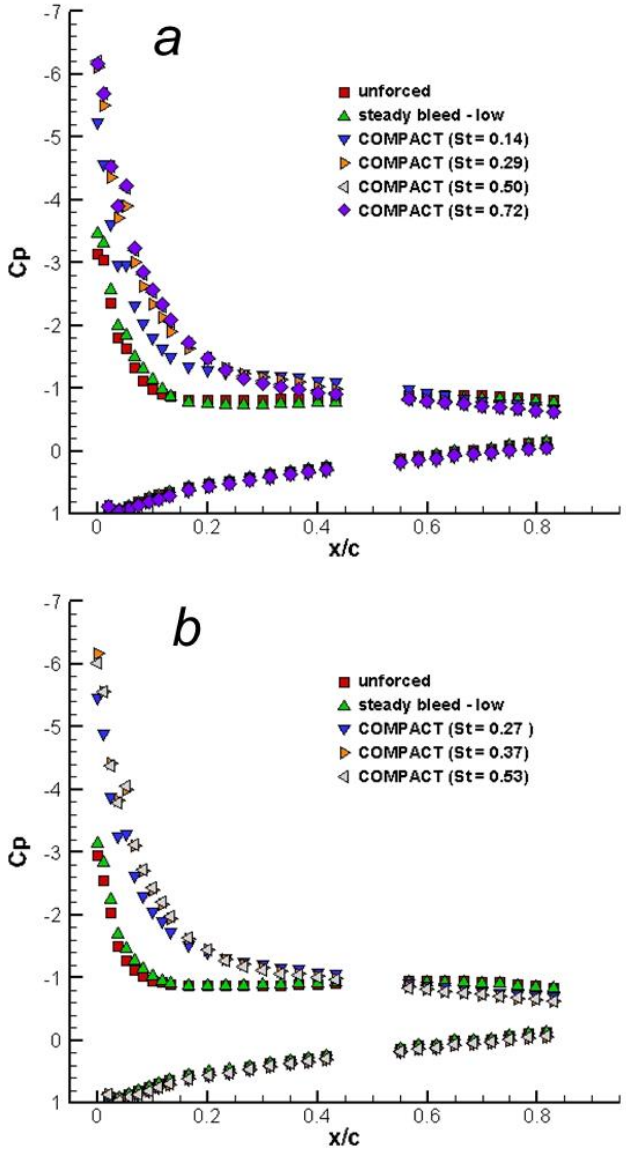

Figure 21. Static pressure distributions along the centerline for tangential actuation for Re=650,000 (a) and 875,000 (b) (α=18°) at a fixed refill rate and several repetition rates St_{act}.

Finally, a representative sample of the centerline pressures with the trip wire removed is shown in Figure 22 (Re= 875,000 and α=18°) for tangential actuation. As noted above, in the absence of the trip the baseline separation is somewhat more unstable. However, the peak pressures achieved by attachment with the COMPACT actuation are the same as in the tripped flow. It is also noted that the small pressure spike observed in the pressure data in the presence of the trip wire (e.g., Figure 19b near x/c = 0.05), is absent in Figure 22.

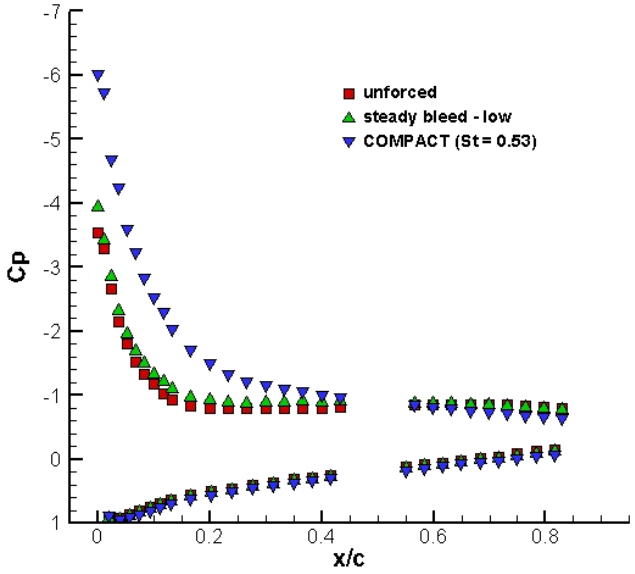

Figure 22. Static pressure distributions along the centerline for tangential actuation with trip wire removed (Re = 875,000, α=18°).

CONCLUSIONS AND RECOMMENDATIONS

As part of a multi-year program focused on investigating the effectiveness of combustion-powered actuation (COMPACT) upon dynamic stall across a range of Mach numbers, high-Mach simulations and low-speed experiments have been carried out. The computational results suggest that COMPACT actuation can result in increased cycle-averaged lift and decreased cycle-averaged drag at Mach 0.3 and 0.4. Effectiveness at Mach 0.5 appears relatively small. At Mach 0.3 and 0.4, slots oriented tangential to the airfoil surface appear much more effective than slots oriented normal to the airfoil surface. Three-dimensional simulations suggest that finite-span slots may result in reduced effectiveness compared to spanwise-continuous or two-dimensional slots. Finally, an initial investigation into the effect of directing a portion of the actuation jet's momentum in the spanwise direction indicates that some additional benefit may be gained.

Low-speed wind tunnel experiments confirm that slots placed at x/c=0.1, where simulations show good Mach 0.3-0.4 benefits, can also be effective at suppressing static stall at Mach numbers less than 0.1. These experiments also confirm that tangential actuation tends to produce greater stall-suppression than normal actuation.

Further computational efforts are required to better understand the three-dimensional effects of the finite-span and skewed slots. Additionally, further parametric variation at high Mach number must be conducted in order to examine whether or not slot orientations are possible which will increase stall-suppression capability at Mach numbers greater than 0.4.

Finally, high-speed dynamic stall testing of this concept must be conducted in order to confirm the effectiveness

shown in the simulations and low-speed experiments. High-speed testing is planned for later stages of this program.

ACKNOWLEDGEMENTS

The authors gratefully acknowledge NASA for their support of this work under contract no. NNC12CA36C. Thanks are extended to Norm Schaeffler, technical monitor and Susan Gorton, rotary wing project leader. Thanks are also extended to Peter Lorber, Sikorsky Aircraft.

REFERENCES

1. Lorber, P.F., Bagai, A., and Wake, B.E., "Design and Evaluation of Slatted Airfoils for Improved Rotor Performance," AHS 62nd Annual Forum and Display, Phoenix, AZ, May 2006.
2. Mishra, A., Ananthan, S., Baeder, J.D., Opoku, D.G., Wake, B.E., and Lin, R.-S., "Coupled CFD/CSD Prediction of the Effects of Leading Edge Slat on Rotor Performance," Annual Forum Proceedings - AHS International, 2009.
3. Kinzel, M.P., Maughmer, M.D., and Lesieutre, G.A., "Miniature trailing-edge effectors for rotorcraft performance enhancement," *Journal of the AHS*, V. 52, No. 2, pp. 146-158, 2005.
4. Singh, C., Peake, D.J., Kokkalis, A., Khodagolian, V., Coton, F.N., and Galbraith, R. A.McD., "Parametric study of an air-jet vortex generator configuration to control rotorcraft retreating blade stall," AIAA-2005-1366, 2005.
5. Lombardi A. J., Bowles, Patrick O., and Corke, T. C., "Closed-Loop Dynamic Stall Control Using a Plasma Actuator," AIAA paper 2012-0918, 50th AIAA Aerospace Sciences Meeting, January 2012, Nashville, Tennessee.
6. Kelley, C. L., Bowles P., Cooney, John, He, Chuan, and Corke, T. C., Osborne, B. Silkey, J., and Zehnle, J., "High Mach Number Leading-edge Flow Separation Control Using AC DBD Plasma Actuators," AIAA paper 2012-0906, 50th AIAA Aerospace Sciences Meeting, January 2012, Nashville, Tennessee.
7. Crittenden., T., Woo, G., and Glezer, A., "Combustion Powered Actuators for Separation Control," AIAA Paper 2012-3135, 6th AIAA Flow Control Conference, New Orleans, LA, June 2012.
8. Funk, R., Crittenden, T., Parekh, D., and Glezer, A., "Transient Separation Control Using Pulse Combustion Actuation," AIAA Paper 2002-3166, 1st AIAA Flow Control Conference, St. Louis, MO, June 2002.
9. Brzozowski, D. and Glezer, A., "Transient Separation Control using Pulse-Combustion Actuation," AIAA Paper 2006-3024, 3rd AIAA Flow Control Conference, San Francisco, CA, 2006.
10. Woo, G., Crittenden, T., and Glezer, A., "Transitory Control of a Pitching Airfoil using Pulse Combustion Actuation," AIAA Paper, 4th AIAA Flow Control Conference, Seattle, WA, 2008-4324, 2008.
11. Woo, G., Crittenden, T., and Glezer, A., "Transitory Separation Control over a Stalled Airfoil," AIAA Paper, AIAA 39th Fluid Dynamics Conference, San Antonio, TX, 2009-4281, 2009.
12. Brzozowski, D., Woo, G., Culp, J., Glezer, A., "Transient Separation Control using Pulse-Combustion Actuation," AIAA J., V. 48, 2482-2490, 2010.
13. Martin, P.B., McAlister, K.W., Chandrasekhara, M.S., and Geissler, W., "Dynamic Stall Measurements and Computations for a VR-12 Airfoil with a Variable Droop Leading Edge," AHS 59th Annual Forum, Phoenix, AZ, May 2003.
14. Lorber, P.F., D. McCormick, B.E. Wake, and R. Florea, "Helicopter Retreating Blade Stall Control," MAFC Panel - AIAA Flow Control Conference, June 25, 2002.